Spatial and temporal melt variability at Helheim Glacier, East Greenland, and its effect on ice dynamics

M. L. Andersen,[1,2] T. B. Larsen,[1] M. Nettles,[3] P. Elosegui,[4] D. van As,[1] G. S. Hamilton,[5] L. A. Stearns,[6] J. L. Davis,[3] A. P. Ahlstrøm,[1] J. de Juan,[4] G. Ekström,[3] L. Stenseng,[7] S. A. Khan,[7] R. Forsberg,[7] and D. Dahl-Jensen[2]

Received 5 May 2010; revised 1 September 2010; accepted 20 September 2010; published 29 December 2010.

[1] Understanding the behavior of large outlet glaciers draining the Greenland Ice Sheet is critical for assessing the impact of climate change on sea level rise. The flow of marine-terminating outlet glaciers is partly governed by calving-related processes taking place at the terminus but is also influenced by the drainage of surface runoff to the bed through moulins, cracks, and other pathways. To investigate the extent of the latter effect, we develop a distributed surface-energy-balance model for Helheim Glacier, East Greenland, to calculate surface melt and thereby estimate runoff. The model is driven by data from an automatic weather station operated on the glacier during the summers of 2007 and 2008, and calibrated with independent measurements of ablation. Modeled melt varies over the deployment period by as much as 68% relative to the mean, with melt rates approximately 77% higher on the lower reaches of the glacier trunk than on the upper glacier. We compare melt variations during the summer season to estimates of surface velocity derived from global positioning system surveys. Near the front of the glacier, there is a significant correlation (on >95% levels) between variations in runoff (estimated from surface melt) and variations in velocity, with a 1 day delay in velocity relative to melt. Although the velocity changes are small compared to accelerations previously observed following some calving events, our findings suggest that the flow speed of Helheim Glacier is sensitive to changes in runoff. The response is most significant in the heavily crevassed, fast-moving region near the calving front. The delay in the peak of the cross-correlation function implies a transit time of 12–36 h for surface runoff to reach the bed.

Citation: Andersen, M. L., et al. (2010), Spatial and temporal melt variability at Helheim Glacier, East Greenland, and its effect on ice dynamics, *J. Geophys. Res.*, *115*, F04041, doi:10.1029/2010JF001760.

1. Introduction

[2] In assessing climate change and its impact on sea level rise, understanding changes in the flow dynamics of large outlet glaciers and ice streams is crucial. Flow speed variations occur on a variety of timescales, from minutes [*Amundson et al.*, 2008; *Nettles et al.*, 2008] to months [e.g., *Luckman and Murray*, 2005; *Joughin et al.*, 2008b] to years [e.g., *Luckman et al.*, 2006; *Howat et al.*, 2007, 2008] and longer. It has recently been established that variations in conditions at the glacier terminus exert an important influence on glacier flow speed in Greenland [e.g., *Amundson et al.*, 2008; *Howat et al.*, 2008a; *Joughin et al.*, 2008c; *Nettles et al.*, 2008; *Nick et al.*, 2009], but less is known about how variations in surface melting influence outlet glacier dynamics. During the annual melt season, a fraction of the meltwater produced at the surface evaporates and a fraction may run off the glacier via supraglacial channels. Part of the meltwater also drains from the surface into the englacial hydrological system through crevasses and moulins. This system is likely to supply water to the bed of the glacier. Changes in this supply may affect the flow of the glacier by increasing the basal water pressure and reducing the effective pressure, creating a lubricating effect at the ice-bedrock interface. Although this effect has been established on alpine glaciers [e.g., *Iken and Bindschadler*, 1986; *Bartholomaus et al.*, 2008], and within the ice sheet [e.g., *Zwally et al.*, 2002; *van de Wal et al.*, 2008], its magnitude on fast-flowing outlet glaciers in Greenland has not been studied extensively. In this study, we focus on the effect of

[1]Geological Survey of Denmark and Greenland (GEUS), Copenhagen, Denmark.
[2]Centre for Ice and Climate, University of Copenhagen, Copenhagen, Denmark.
[3]Lamont-Doherty Earth Observatory, Columbia University, New York, New York, USA.
[4]Institute for Space Sciences, CSIC, IEEC, Barcelona, Spain.
[5]Climate Change Institute, University of Maine, Orono, Maine, USA.
[6]Department of Geology, University of Kansas, Lawrence, Kansas, USA.
[7]DTU-Space, Technical University of Denmark, Copenhagen, Denmark.

0148-0227/10/2010JF001760

runoff on the flow of Helheim Glacier, a large outlet glacier in East Greenland.

[3] Melt studies conducted on glaciers have used a variety of techniques, depending on the timescale and available data. A frequently used technique is the positive degree-day (PDD) model, which employs a correlation between melt and periods with above zero mean air temperatures [e.g., *Reeh*, 1991; *Braithwaite*, 1995]. PDD methods require minimal input data and are therefore suitable for large areas and long timescales since few parameterizations need be made. *Hanna et al.* [2005] applied this technique to calculate runoff for the entire Greenland Ice Sheet at 5 × 5 km resolution and *Huybrechts et al.* [1991] used the PDD method to project runoff for future warming scenarios. An alternative, physically based, approach is to calculate the surface energy balance (SEB) and thus quantify the energy available for melt at the surface [*Hock*, 2005]. Due to the greater requirement for observational input data, energy-balance models typically are run for short timescales and small areas, although *van de Wal and Oerlemans* [1994] constructed an energy-balance model for the entire Greenland Ice Sheet at 20 km resolution. Recent work (modeling as well as in situ observations) has increased the performance and resolution of large-scale energy-balance models through improvements of regional climate models. These models can include an energy-balance model at the ice-atmosphere boundary, as in the case of *Ettema et al.* [2009], which describes model runs over the Greenland Ice Sheet with an 11 km resolution.

[4] Most of what is known about the general velocity behavior of glaciers in Greenland comes from space-based remote sensing studies, either for the whole ice sheet perimeter [e.g., *Rignot and Kanagaratnam*, 2006] or for specific glacier catchment basins [e.g., *Stearns et al.*, 2005; *Luckman et al.*, 2006; *Howat et al.*, 2007, 2008a; *Joughin et al.* 2008a]. A limitation of this approach is the low temporal resolution of most remote sensing products.

[5] Ground-based melt and velocity studies have been conducted in Greenland by several authors, although almost exclusively on the ice sheet, not on outlet glaciers. *Zwally et al.* [2002] found indications of an association between surface generated meltwater and the velocity of the ice sheet near Swiss Camp, north of Jakobshavn Isbræ. Near Kangerlussuaq, South West Greenland, *van de Wal et al.* [2008] observed velocity variations of up to 30% along the *K-transect* during the 2005–2006 melt season. In the same area, *Shepherd et al.* [2009] found increases of ice sheet flow speed of up to 35% per positive degree-day of melting. While ground-based methods typically have very high temporal resolution, they suffer from the lack of spatial coverage of space- or airborne remote sensing techniques.

[6] *Joughin et al.* [2008b] combined field observations with remote sensing data and noted a large and widespread influence of surface meltwater on ice sheet velocity, with smaller variations in outlet glacier velocity resulting from meltwater lubrication. Those authors observed seasonal velocity increases of 50–100% (36–71 m yr^{-1}) on the ice sheet and 9–14% (51–77 m yr^{-1}) on regions defined as outlet glaciers.

[7] Little is known about short-term velocity variations in outlet-glacier flow. *Amundson et al.* [2008] and *Nettles et al.* [2008] established a correlation between calving events and glacier acceleration at Jakobshavn and Helheim glaciers. However, no comprehensive study has investigated the link between changes in melt rates and near-terminus velocity variations on fast outlet glaciers. As the climate warms, understanding the influence of meltwater becomes increasingly important for estimates of sea level rise. In addition to the direct effect of added freshwater runoff into the oceans, indirect effects such as the influence of meltwater on ice flow speed must be considered.

[8] Here, we develop a surface-energy-balance model for Helheim Glacier in East Greenland, utilizing data recorded by an automatic weather station (AWS) deployed on the glacier. We compare the pattern of melt variability derived from the SEB model with a velocity record derived from global positioning system (GPS) observations to assess the influence of daily variations in melt volume on glacier flow speed.

2. Data and Methods

[9] This study combines an observational and a modeling approach to study the effect of glacier melt variability on glacier dynamics. The observational component includes data from an AWS we deployed on the trunk of Helheim Glacier during the summers of 2007 and 2008, a network of 12–22 continuously operating GPS receivers also deployed across Helheim Glacier during the summers of 2007 and 2008, and standard stake-based ablation point measurements made at the locations of the GPS stations during their deployment, servicing, and retrieval (Figure 1). We use the AWS data to calibrate and drive a SEB model for the snow-free ablation area of Helheim Glacier and use this model to predict melt variations across the glacier during the summer seasons of 2007 and 2008. We then perform a cross-correlation analysis with the GPS velocity records to assess the influence of melt variations on glacier speed.

2.1. Surface-Energy-Balance Model

[10] We construct a surface-energy-balance model for the snow-free ablation area of Helheim Glacier, first developing the SEB model for a single point, corresponding to the location of our AWS. We then distribute the model across the glacier as described in section 2.2 below.

[11] We quantify melt by determining the budget of energy fluxes to and from the surface, following standard methods [e.g., *van de Wal and Oerlemans*, 1994; *Hock*, 2005; *Hock and Holmgren*, 2005; *van As et al.*, 2005; *van den Broeke et al.*, 2008]. In our case, the energy flux available for melt, Q_M, is determined by the balance of the terms of the energy flux budget at the surface:

$$Q_M = Q_H + Q_E + Q_G + L_{SW} + L_{LW} + Q_R, \quad (1)$$

which is calculated in hourly time steps.

[12] The sensible heat flux, Q_H, is the turbulent transfer of heat resulting from a temperature difference between the surface and near-surface atmosphere. The latent heat flux, Q_E, is a function of the near-surface atmospheric vapor gradient and wind speed, giving the heat loss/gain caused by sublimation and evaporation.

[13] Q_G is the subsurface heat flux, i.e., heat conducted to or from the surface through the ice column below. L_{SW} and

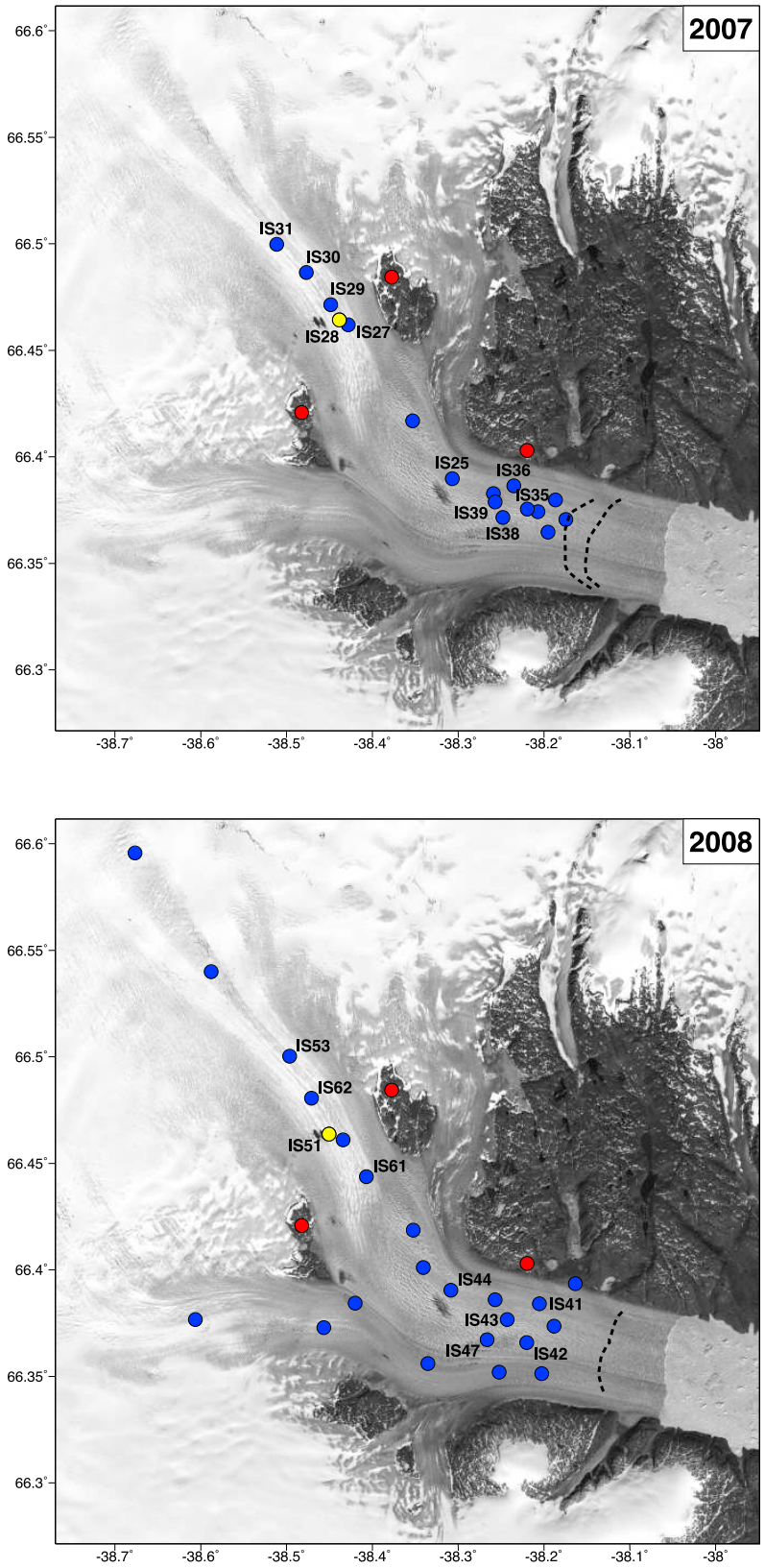

Figure 1. Map of both AWS and GPS deployments in 2007 and 2008 overlain on a 2001 LANDSAT image. Dots mark the position of (blue) GPS ice sites, (yellow) colocated AWS and GPS sites, and (red) GPS reference sites. GPS sites mentioned in the text are labeled. Dotted lines are calving front positions on 4 July 2007 (westernmost) and 24 August 2007, both from MODIS 250-m images, and 31 July 2008 from field observations.

L_{LW} are the net short-wave and long-wave radiative energy fluxes, respectively. Q_R is the energy added to the surface by rainfall, which in our case is set to zero, due to a lack of necessary data (see section 2.1.2 below). The sign convention dictates that energy fluxes into the surface are positive, while fluxes directed away from the surface are negative.

[14] The net short-wave flux, L_{SW}, is the difference between the measured incoming short-wave radiation at the AWS and the reflected short-wave radiation found by applying an albedo value at each time step, as described below. The net long-wave radiation, L_{LW}, is the difference between the incoming long-wave radiation measured at the AWS and the outgoing long-wave radiation calculated from the modeled surface temperature at each time step, assuming black-body properties.

[15] The bulk aerodynamic method assumes that Q_H is a function of the air temperature gradient and that Q_E is a function of the humidity gradient. In addition, both fluxes are proportional to wind speed. Assuming Monin-Obukhov similarity, the turbulent fluxes, Q_H and Q_E, can be approximated as:

$$Q_H = \rho c_p u_* \theta_*, \tag{2}$$

$$Q_E = \rho L_v u_* q_*, \tag{3}$$

where ρ is the air density, c_p is the specific heat capacity of air, and L_v is the latent heat of sublimation.

[16] The friction velocity, u_*, in equations (2) and (3) is given as:

$$u_* = \frac{k u_{z_w}}{\ln\left(\frac{z_w}{z_0}\right) - \psi_{m2} + \psi_{m1}}, \tag{4}$$

where k is Von Karman's constant, u_{z_w} is measured wind speed at height z_w, and z_0 is the roughness length scale for momentum. ψ_{m1} and ψ_{m2} are momentum stability correction functions.

[17] The virtual potential temperature scale, θ_*, in equation (2) is:

$$\theta_* = \frac{k(\theta_v - T_s)}{\ln\left(\frac{z_{tmp}}{z_t}\right) - \psi_{h2} + \psi_{h1}}, \tag{5}$$

where z_{tmp} is the height at which temperature is measured, z_t is the roughness scale for temperature, θ_v is the virtual temperature, and T_s is the surface temperature. ψ_{h1} and ψ_{h2} are temperature stability correction functions.

[18] The turbulent scale of humidity, q_*, in equation (3) is given by:

$$q_* = \frac{k[q(z_{hum}) - q(0)]}{\ln\left(\frac{z_{hum}}{z_q}\right) - \psi_{q2} + \psi_{q1}}, \tag{6}$$

where z_{hum} is the height at which humidity is measured and z_q is the roughness length scale for humidity. ψ_{q1} and ψ_{q2} are humidity stability correction functions.

[19] The stability correction functions ψ_{m1}, ψ_{m2}, ψ_{h1}, ψ_{h2}, ψ_{q1}, and ψ_{q2} in equations (4), (5), and (6) are adopted from *Paulson* [1970] and *Holtslag and De Bruin* [1988] for stable and unstable conditions, respectively.

[20] We calculate the subsurface heat flux, Q_G, using a one-dimensional finite difference solution of the heat equation, such that the energy flux to the surface from the first layer below the surface is proportional to the temperature difference between the two layers. Q_G-energy fluxes are calculated at 15 min intervals for 200 layers, each 0.05 m thick, i.e., for a 10 m deep ice column. The layer thickness is chosen to provide sufficient resolution to represent small vertical variations while the number of layers is chosen to ensure that the base of the column is only weakly affected by diurnal variations and to keep calculations stable. The top layer in the ice column is fixed at the modeled surface temperature at each time step and the bottom layer has the temperature of the layer immediately above it. The bottom boundary condition implies that we only evaluate the effect of heat storage and release in the upper ice column. The net transfer to and from the deeper glacier is not considered. The model is initialized using an observed summer temperature profile from the TAS-U station maintained by the Programme for Monitoring of the Greenland Ice Sheet (PROMICE; http://www.promice.dk) at a site ~100 km south of Helheim Glacier and at a similar altitude to our AWS. The effective conductivity is assumed constant in ice and set to 2.2 WK^{-1} m^{-1}. The ice density is set to 917 kg m^{-3}.

[21] Short-wave penetration into the ice causing subsurface heating, and possibly melt, cannot be ignored over a melting ice surface [e.g., *van den Broeke et al.*, 2008]. For the short-wave fraction not reflected by the surface we therefore apply an exponential absorption for the flux in the ice column, according to Beer's law with an extinction coefficient of 1.4 for ice [*Greuell and Konzelmann*, 1994]. The resulting contribution is added to the temperature profile used in the solution of the heat equation described above. In cases where the subsurface temperature reaches the melting point, we calculate melt from the excess energy flux and add this to the melt produced at the surface.

[22] The surface temperature, T_s, is the only remaining unknown parameter. Following, for example, *van den Broeke et al.* [2008], we determine T_s by an iterative process in each time step, assuming balance in the energy budget. For solutions in which $T_s > 0$°C, T_s is set to the melting point, leaving a residual energy flux available for melt (if $Q_M > 0$).

[23] With the quantities in the energy budget determined, the corresponding surface ablation rate, M, (in m s^{-1}) is

$$M = \frac{Q_M}{\lambda \rho_{ice}}, \tag{7}$$

where λ is the latent heat of fusion (3.35×10^5 J kg^{-1}) and ρ_{ice} is the density of ice. The meltwater generated by ablation in the model is assumed to run off the surface instantaneously.

2.1.1. AWS Observations

[24] We drive the surface-energy-balance model using meteorological measurements recorded at Helheim Glacier. We deployed an AWS on a relatively slow-moving section (~12 m d^{-1}) of the glacier trunk (Figure 1). The AWS collected continuous data (Figure 2) at a rate of one sample per hour for a total of 27 days in the summer of 2007 and 49

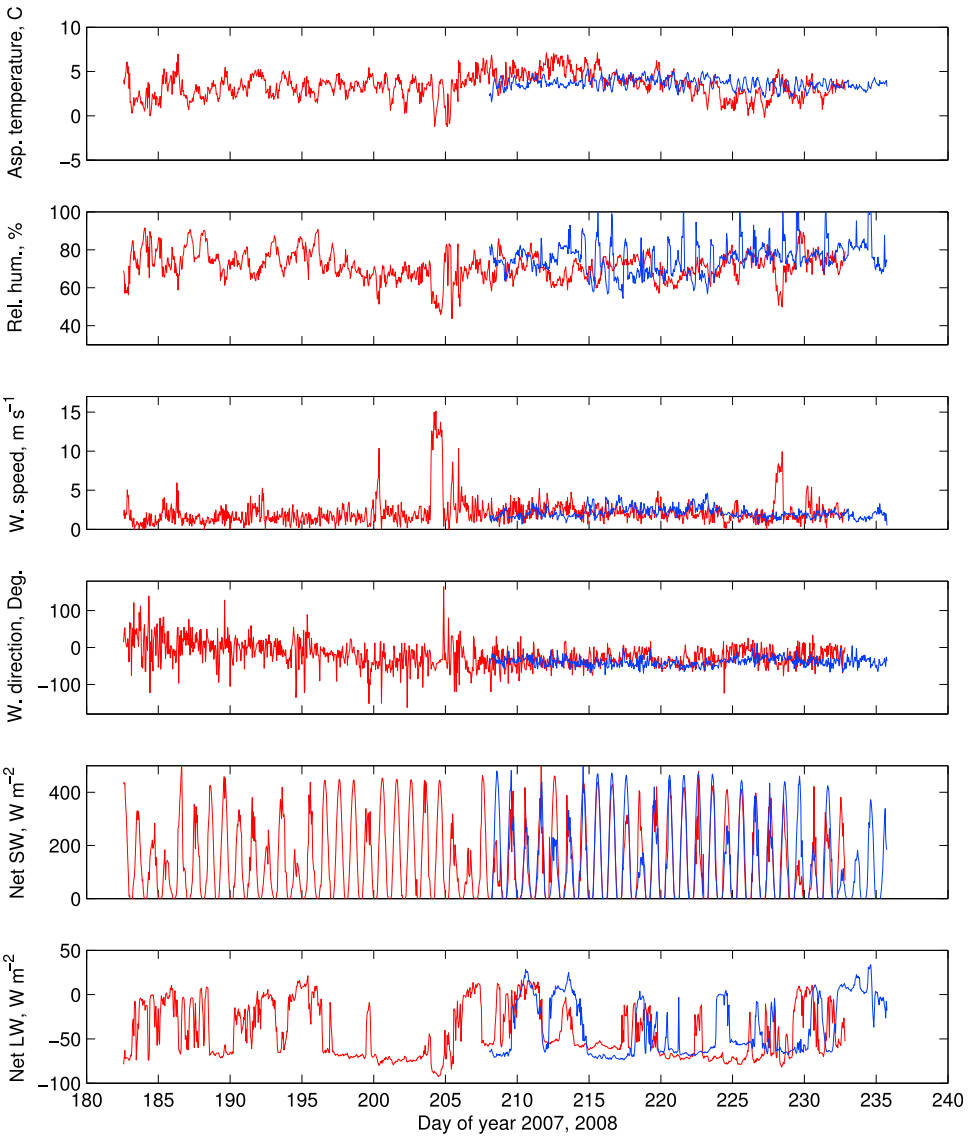

Figure 2. Time series of meteorological parameters measured by the AWS in (blue) 2007 and (red) 2008. Aspirated temperature is modeled for 2007 (see text). Wind direction is plotted in the interval [−180, 180] degrees from N with positive values increasing clockwise.

days in the summer of 2008. To facilitate interannual comparisons, we endeavored to occupy approximately the same glacier location with the AWS during both deployments. The station locations (approximately 66.42°N, 38.44°W, 640 m above sea level), were within 650 m distance and 20 m elevation of each other, with the second year lower than the first.

[25] The AWS recorded standard meteorological parameters, including wind speed and direction, aspirated air temperature, ice surface height, short- and long-wave radiative fluxes (incoming and reflected), station tilt, and surface ablation. Wind speed and direction were measured with a Young 05103-5 wind vane; aspirated temperature and relative humidity were measured using a combined fan ventilated Rotronic PT100 temperature probe and an S3 hygroclip, accurate to 0.1 K and 1%, respectively. Radiative fluxes were measured with a Kipp & Zonen CNR1 net radiometer with a specified accuracy of 10% on daily totals. Sensors were mounted on a tripod at heights of 2.8–3.2 m. The untethered AWS lowered with the ablating surface. The surface ablation measurement is crucial for evaluating the SEB model performance and was made on a separate rig with stakes drilled >5 m into the ice to avoid self-drilling. Snow height and ablation were measured with two Campbell SR50 sonic rangers, each accurate to 1 cm.

[26] The air density, ρ_{air}, a parameter in the turbulent flux calculations, depends in part on the barometric pressure. Barometric pressure was not measured at the AWS, but daily values measured in the nearby town of Tasiilaq (~100 km from Helheim glacier) are available from the Danish Meteorological Institute (http://www.dmi.dk/dmi/index/gronland/vejrarkiv-gl.htm). These measurements were interpolated linearly in time to obtain hourly values and were then spatially extrapolated to the station altitude using the barometric

equation. When the DMI record was incomplete, missing values were set to mean values of the past 5 years for the day in question.

[27] Measurements of near-surface air temperature and ablation were not acquired in 2007 due to instrument malfunctions. The temperature record for 2007 was therefore reconstructed using the casing temperature from the CNR1 radiometer, which operated throughout the season. A simple equation relating observed aspirated air temperature, T_{asp}, to casing temperature T_{CNR1}, short-wave radiation SW_{in}, and wind speed U was used

$$T_{asp} = aT_{CNR1} + bSW_{in} + cU + d \quad (8)$$

and a least-squares solution was found using the 2008 data. The solution yielded coefficients a, b, c, and d that were then used to calculate an aspirated temperature record for 2007 (shown in Figure 2). For the 2008 record the postfit root-mean-square (RMS) residual was 1 K, approximately one order of magnitude larger than the quoted error of the PT100 temperature probe (0.1 K). This residual represents 13% of the range of the values measured (8.3 K). We adopt the value of 1 K as an estimate of the error for the reconstructed 2007 temperature record and include this record in our analysis. Independent ablation measurements at the AWS also failed during almost all of 2007, leaving only one automatically measured value at the end of the time series available for model validation. Hourly data values were successfully acquired for all other parameters.

[28] Prior to implementation in the SEB model, the data are edited for gaps and outliers. Incoming short-wave radiation measurements are sensitive to the tilt of the instrument and are therefore corrected based on tilt measurements using a standard algebraic transformation [e.g., *MacWhorter and Weller*, 1991]. We also perform a number of other standard corrections, including correction of the sonic ranger ablation measurements for variations in the speed of sound with air temperature. The measured albedo at the AWS site is also smoothed with a running ±12 h average.

2.1.2. Perturbation Analysis for SEB Error Assessment

[29] Errors in the SEB model arise from measurement errors in the input data and inaccuracies in assumptions made in the model calculations. Following *van As et al.* [2005], we use a simplified sensitivity analysis to characterize the effect of parameter perturbations on SEB model output. Specifically, we alter all measured values (relative humidity, net short-wave flux, net long-wave flux, aspirated temperature, wind speed and direction, and barometric pressure) with the quoted uncertainties from the instrument documentation, positive and negative, about the measured values. We do this with one parameter at a time while fixing all remaining parameters to unperturbed values, for all GPS station locations and the AWS site, and record the difference with respect to the unperturbed model solution. For each location, we thereby generate a set of 14 perturbed melt model outputs (i.e., two per each of the seven measurable parameters above), which we group into those yielding more melt than the unperturbed solution and those yielding less melt. Upper and lower error bounds on the melt are then calculated by forming, independently for each (positive and negative) group, the RMS of the residuals of the perturbed melt outputs relative to the unperturbed model melt solution. The resulting (positive and negative) errors thus calculated are not exactly symmetric because the SEB model is not linear on the perturbed parameters, because of the small-number statistics involved, or both. (A fully comprehensive error analysis such as in a Monte Carlo-type simulation is deemed unnecessary.)

[30] In our analysis the net short-wave component is perturbed with the ±10% value provided by Kipp & Zonen as the uncertainty for daily totals measured with the CNR1 net radiometer. However, *van den Broeke et al.* [2004], testing the same sensor, found the actual error value to be <5%. The application of maximum perturbation values and the method of accumulating the errors in each time step leads to a conservative (i.e., large) error estimate for each time step and for the cumulative melt, with the maximum error always carried over from one time step to the next.

[31] Energy added to the surface by rainfall is not included due to the lack of a precipitation record from Helheim Glacier. A sensitivity study using the Tasiilaq rain record was performed and revealed very low energy fluxes (mean contribution to the energy budget was ~0.25 W m^{-2}). We therefore do not include this effect, nor do we consider the added runoff caused by rainwater. While the added runoff from rainfall has been shown to affect sliding velocity [e.g., *Howat et al.*, 2008b], applying the Tasiilaq precipitation record at Helheim Glacier is not justified. Anecdotal field observations show strongly changing weather conditions over the ~100 km between the locations.

2.2. Distributed Surface-Energy-Balance Calculations

[32] We distribute the SEB spatially by discretizing the glacier surface in 500 × 500 m model cells, and calculating the energy flux available for melt (Q_M) in each cell. The distributed SEB model is run for the full periods for which data are available for 2007 and 2008 (days of year 208–235 for 2007 and days of year 182–232 for 2008). All cells within the model domain with altitudes above 1000 m above sea level, or located on rock outcrops, are masked to isolate the potential melt area. All cells are assumed snow free (i.e., not contributing to runoff by way of snowmelt). Field observations from early July 2008 (at the beginning of the data collection, which was earlier than in 2007) support this assumption.

2.2.1. Digital Elevation Model

[33] Several of the input parameters for the SEB model are altitude dependent. We obtain altitudes for the model cells using a digital elevation model (DEM) of Helheim Glacier constructed using the method described in *Stearns and Hamilton* [2007]. We use an ASTER image acquired on 30 August 2006 and smoothed to 500 m grid spacing, using nearest-neighbor interpolation.

[34] Geolocation information is derived from the satellite ephemeris information contained in the image header file and has an uncertainty of approximately 50 m. The DEM uncertainties are a combination of systematic errors and random errors due to satellite positioning, image acquisition geometry, and atmospheric conditions. Elevations from GPS point measurements on Helheim Glacier made at the time of the 30 August 2006 image acquisition are used to assess the accuracy of the ASTER DEM [*Stearns*, 2007]. The absolute elevation error (RMS difference) of the 30 August 2006 DEM is 16.9 m, most of which is due to a systematic bias in

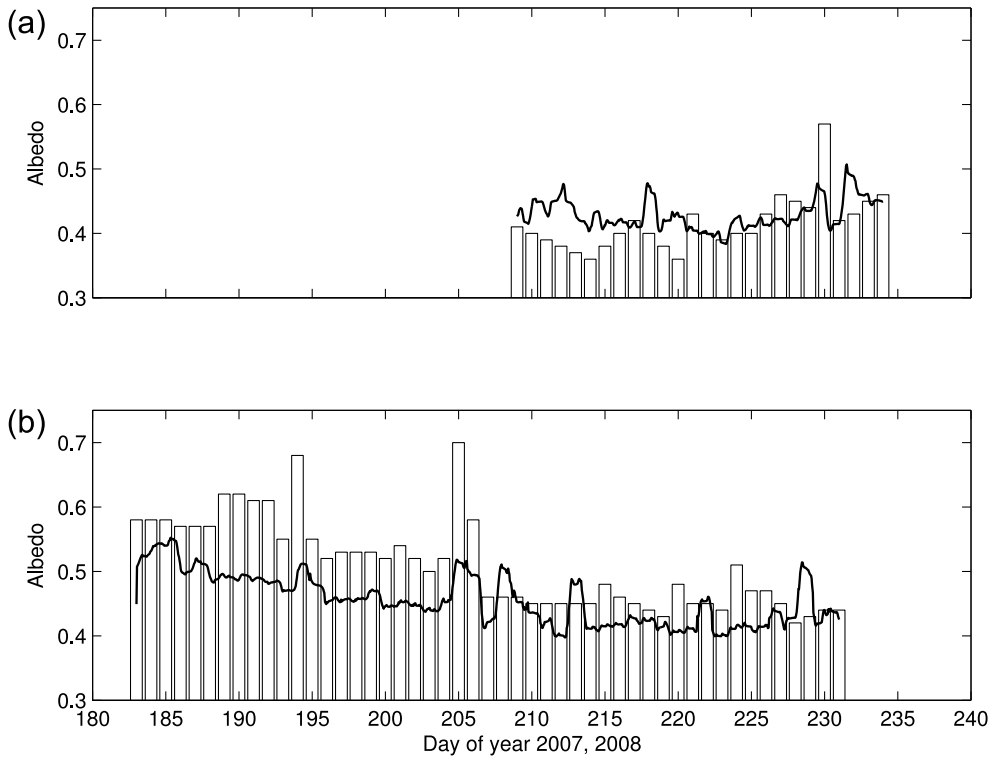

Figure 3. (Bars) MODIS derived and (curve) measured albedos in (a) 2007 and (b) 2008 in the model cell where the AWS was deployed.

the DEM. When this bias is removed, the RMS difference drops to 6.5 m.

2.2.2. Albedo

[35] A large component of the total energy budget is the net short-wave energy flux, L_{SW}, which is the sum of the incoming and the reflected short-wave radiation. The incoming component was measured at the AWS and is assumed uniform across the model domain. The reflected component is determined from multiplication of the incoming component with the reflectivity (albedo). We acquire daily albedo values for all model cells in the grid using Moderate Resolution Imaging Spectroradiometer (MODIS) observations. For 2007 and 2008, 44 and 58 scenes are selected from the MOD10A1 Daily Snow Albedo product [*Hall et al.*, 2007, 2008], respectively. To avoid extrapolation near the beginning and end of the experiment, scenes from outside the deployment periods are also included. The selected scenes are reprojected onto an equal-area regular grid for analysis. Daily values are thus acquired on a cell-by-cell basis. In the case of partly cloud-covered images, which cause occasional data gaps for one or more cells, values are linearly interpolated in time from the last known albedo value of the relevant cell. The longest data gaps are 4–5 consecutive days for the majority of the model domain. Helheim Glacier exhibits large spatial variations in albedo caused by highly crevassed areas and meltwater lakes. By using the position-specific values from the MODIS pixels we capture this variation in the model to within a 500 × 500 m resolution.

[36] *Stroeve et al.* [2006] evaluated the accuracy of the MOD10A1 albedo product. They found that in the accumulation zone there was a good correlation with field observations, while in the ablation zone, the correlation was somewhat lower. In a few particular instances, we observe daily differences between MODIS and observed albedo of up to ~20% with the MODIS pixel having an unrealistically high value. However, an analysis of albedo for the cell containing the AWS reveals an average difference between measured and MODIS derived albedo of only ~3% for 2007 and ~6% for 2008 (Figure 3). A possible source of this offset is the difference in spatial averaging between the point measurement at the AWS and the 500 × 500 m MODIS tile. It is unclear why the higher MODIS values are most pronounced early in the season, although the changing solar angle during the measurement period may play a role, as discussed by *Stroeve et al.* [2006]. The correlation between the MODIS albedo, interpolated to hourly values, and the ±12 h smoothed albedo measured by the AWS is significant at >95% levels, indicating that the temporal variation in the signal is captured well.

2.2.3. Other Parameterizations

[37] The DEM derived altitudes are used to parameterize values of aspirated near surface air temperature T_{asp}. We use an adiabatic lapse rate of 6.3 K km^{-1} based on an average of June, July, and August lapse rates from eight transects along the Greenland Ice Sheet [*Mernild et al.*, 2008]. Values for the roughness length for momentum, z_0, have large variability in the literature. *Brock et al.* [2006] find values for z_0 in the range 0.92–5.47 mm for an alpine glacier while *Munro* [1989] finds a value of 2.44–2.48 mm for glacier ice. *Meesters et al.* [1997] determine a value of 0.3 mm for a melting Greenland ice surface, while *Greuell and Konzelmann* [1994] observe z_0 =

3.2 mm for the Swiss Camp location on the West Greenland ice sheet. We have no direct knowledge of the spatial or temporal variation of z_0 across Helheim Glacier so instead we calibrate z_0 to the value of 4 mm, which is consistent with cited values and matches the measured and modeled ablation at the AWS site (see section 3.1.1).

[38] As in *Hock and Holmgren* [2005], relative humidity (RH) is assumed homogenous across the glacier and set to the value measured at the AWS. Given the spatial scale of the glacier (the total modeled area is ~515 km^2), and the common surface characteristics (melting ice) in all cells, this assumption should be reasonable. In addition, RH over a melting ice surface is expected to be close to saturation most of the time, counteracting large vertical gradients.

[39] Incoming long- and short-wave radiation is also assumed to be uniform across the model domain. However, in each time step the incoming short-wave radiation for all model cells is corrected for shading from surrounding topography and surface element azimuths facing away from the sun, again based on the DEM.

[40] Wind speed in the model cells is affected by local topography, providing sheltered as well as exposed areas. Given the topographic variability within the model domain, and that we only have wind speed observations from one point on the glacier, we opt to apply a simple, slope- and curvature-dependent parameterization of wind speed as described in *Liston and Elder* [2006]. The process adjusts the wind speed in each time step for all model cells, depending on the wind direction relative to the terrain slope, slope azimuth, and curvature.

2.3. Stake Measurements

[41] During the deployment of GPS receivers, we embedded aluminum stakes into the ice at each site. The stakes were drilled to a depth of 3 m to minimize additional self-drilling. Exposed stake heights were measured during installation, during a midseason servicing visit, and during retrieval. These measurements yield average melt rates over the periods between observations. In most cases each site had two stakes installed for the main part of the deployment, providing two values, which we average here.

[42] The accuracy of our observations is significantly lower than with usual stake experiments. This error arises from the field conditions, in particular the tendency of the hollow, noncapped aluminum stakes to melt into the hole walls and tilt, effectively lowering the observed melt rate. Moreover, the stake measurements are not from randomly chosen sites and are not necessarily representative of the model cell in which they were placed. Field safety considerations dictated site selection, with the mostly flat, exposed surfaces contributing to the nonrandom nature of the stake sites. On a smaller scale, irregular surface conditions around the stakes also introduce a potential measurement error. In some cases measured heights for two stakes at the same site yielded melt rates up to 30% different. Therefore, while we make a quantitative comparison between stake heights and modeled melt rates, we also assign a relatively high uncertainty of 30% to the stake data.

2.4. Glacier Surface Velocity

[43] We deployed a network of 12–22 continuously recording GPS receivers on Helheim Glacier during the summers of 2007 and 2008 for 54 days and 55 days, respectively. Dual-frequency Trimble 5700 and NetRS receivers collected data at sampling intervals of 1–5 s. Daily velocities were calculated by fitting a linear model to position estimates determined kinematically, as described in *Nettles et al.* [2008]. Each season's network extended over the length of the glacier trunk, including locations within a few km of the calving front (Figure 1).

[44] For this study, several processing steps are performed on the daily velocity time series for 2007 and 2008. The largest changes in daily glacier velocity are associated with glacial earthquakes [*Nettles et al.*, 2008] and appear in the record as step-like increases in velocity on the days of the earthquakes. In order to assess the influence of melt, we subtract this increase (i.e., the velocity difference between the day of the earthquake and the next) from all days following an earthquake in the GPS velocity record. We then remove the mean, and a single, best-fitting linear trend from the time series for each GPS station; the latter accounts approximately for the effects of advection of the station through the glacier flow field. While more sophisticated techniques could be employed for detrending the data [e.g., *Amundson et al.*, 2008] this simple method is adequate for our current analysis.

[45] For the dates on which maintenance visits occurred, we substitute the average speed from the days before and after to avoid incorporating artificial antenna displacements. In cases of data gaps, we assign the mean station velocity of the season. Uncertainties for the velocity estimates are approximately 0.1 m d^{-1} [*Nettles et al.*, 2008].

[46] To simplify our analysis, we distinguish between stations near the front (downstream) and those farther upstream. A cross correlation of daily velocity estimates between 2007 front stations IS25, IS35, IS36, IS38, and IS39 (see map in Figure 1a) demonstrates sufficient similarity between records that we can select one station record as representative of this area. An average correlation coefficient of 0.78 (significant at the 95% level or higher) is found when correlating IS25 with IS35, IS36, IS38, and IS39, respectively. Therefore, IS25 is picked as representative for the front stations, since it has the longest record. A similar spatial pattern is observed for 2008, where we find average correlation coefficients of 0.97 when correlating the front station IS41 with IS42, IS43, IS44, and IS47. Hence, IS41 is picked as representative for front velocity behavior for 2008.

[47] Unlike the downstream stations, melt records from upstream stations (2007: IS27, IS28, IS29, IS30, IS31; 2008: IS51, IS53, IS61, IS62) are somewhat dissimilar (not shown), perhaps due to their larger altitude difference. Therefore, individual stations of interest are selected for comparison with the melt signal.

3. Results

3.1. Validation of SEB Model

[48] To evaluate the SEB model, in this section we first analyze the atmospheric conditions and melt at the AWS site and then compare the SEB melt rates with in situ, stake-based measurements of ablation.

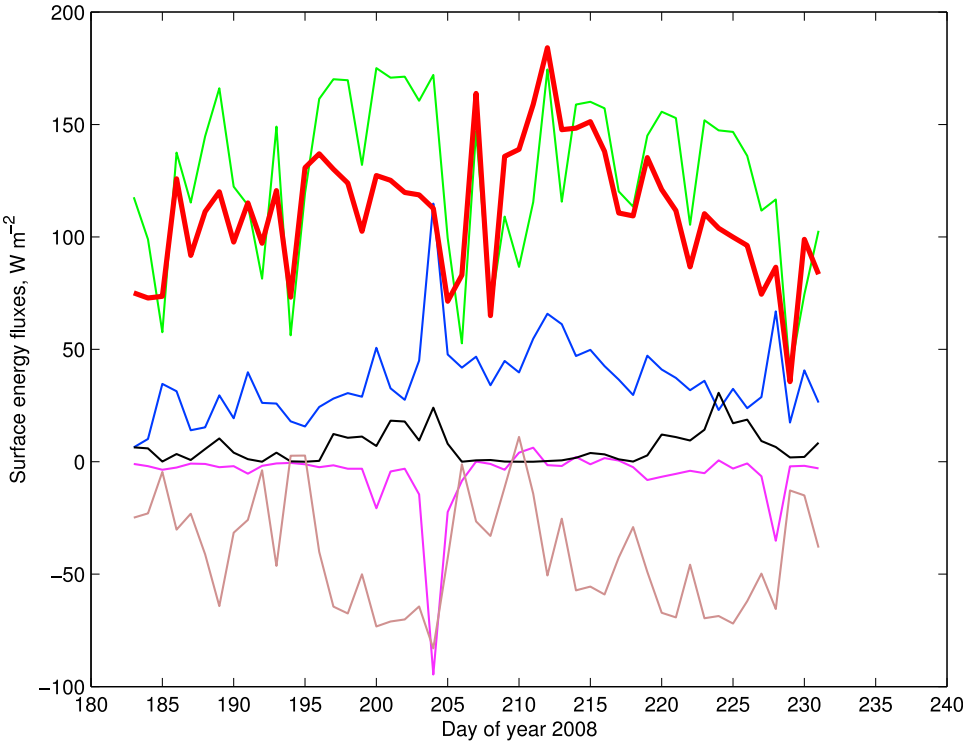

Figure 4. Daily average surface energy fluxes in 2008 at the AWS site for (blue) sensible heat, (purple) latent heat, (black) subsurface heat, (green) net short-wave radiation, (brown) net long-wave radiation, and (red, bold) total energy flux available for melt (see equation (1)).

3.1.1. Meteorological Conditions and Melt at the AWS Site

[49] Values measured at the AWS show many similarities between 2007 and 2008 and some notable differences (Figure 2). The relative humidity measured in 2007 exhibits a daily cycle that is not evident in 2008, except in days 193–198 with a some what lower amplitude. The wind speed is comparable for the 2 years and aspirated temperatures are also similar for both years, even though the 2007 temperature record was synthesized, not observed, as described above in section 2.1.1. The net short-wave radiation is slightly higher in 2007 than 2008, indicating more frequent clear skies. Measurements of net short-wave radiation from both years follow the expected daily cycle. Amplitudes of 2007 net long-wave radiation resemble those observed in 2008.

[50] In 2008 an anomaly occurs on day 204, lasting for 17 h (01:00–18:00 UTC). During this period, the hourly averaged wind speed reaches ~15 m s^{-1}. Low relative humidity values and the lowest aspirated air temperatures of the 2008 experiment were recorded during this time interval, indicating a katabatic wind event. The mean wind direction during this period is 315°, which is not an anomaly but supports this interpretation. During this event, the large-scale atmospheric forcing was most likely aligned with the common katabatic force, favoring stronger winds than usual within the period. No similar events were observed for 2007.

[51] The average daily energy fluxes calculated from the SEB for the AWS site in 2008 are shown in Figure 4. The katabatic wind event on day 204 is clearly seen in the sensible and latent heat fluxes. There is a strong increase in sensible heat flux as a consequence of above average wind speed, and the latent heat flux drops due to the lower humidity gradient over the surface. In spite of high net short-wave and sensible heat fluxes, melt is generally low during this event, since the positive fluxes are balanced by the strongly negative latent heat flux.

[52] The net short-wave flux is a large component in the flux budget (Figure 4) so it is not unexpected that the available melt energy flux Q_M is closely correlated with the net short-wave radiative flux L_{SW}. Maximum melt in 2008 occurs on day 212 after a period of 4 days with increasing melt.

[53] A total ablation of 1.59 m is modeled at the AWS site for 2008 over the ~50 days of observation. For 2007 the total modeled melt for the 27 day deployment is 0.89 m. Considering only the days of year where the two records overlap, this yields similar melt rates for the 2 years of ~3.2 cm d^{-1}.

[54] The SEB model's performance in the grid cell occupied by the AWS in 2008 is shown in Figure 5. The choice of z_0 = 4 mm described in section 2.2.3 minimizes the average difference between measured and modeled ablation, but does not change the shape of the melt curve. The shapes of the melt curves match well, indicating satisfactory performance in capturing changes in melt rates over the season. Figure 5b shows the difference between modeled and measured melt throughout the 2008 deployment. The largest difference occurs on day 222, when the observed

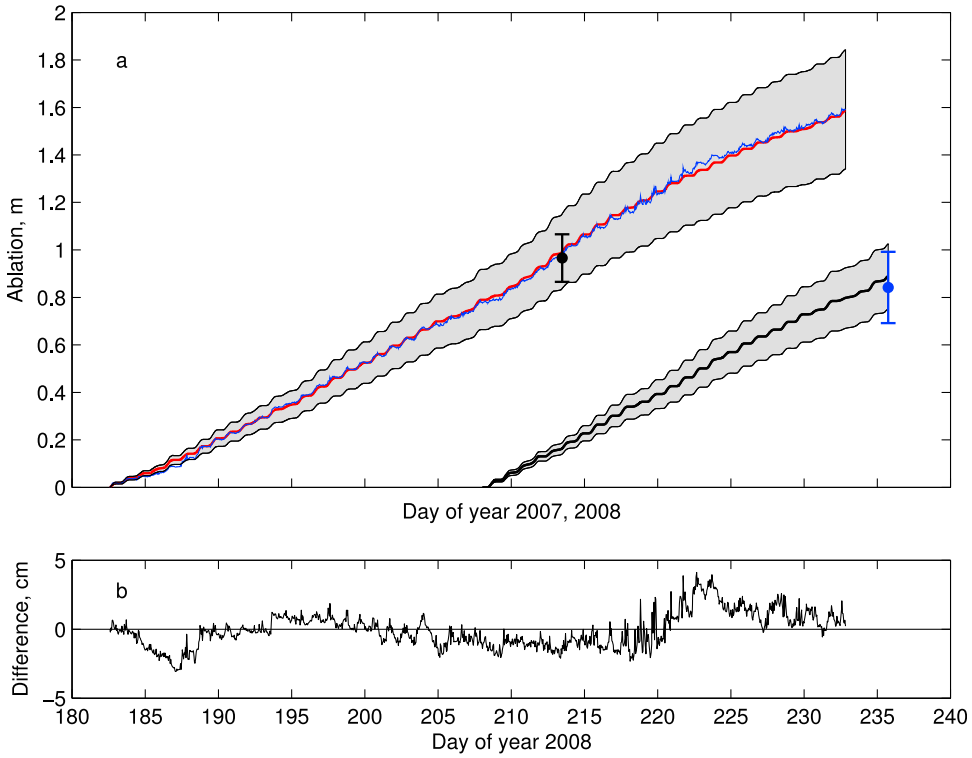

Figure 5. (a) Ablation at model cell corresponding to AWS location. Cumulative ablation for (red) 2008, as calculated by the model, (blue) ablation measured, 2008, by the sonic ranger. Curves are very similar and overlie each other. Black dot with ±10 cm error bar is an independent stake measurement of ablation made on a field visit on day 213, 2008. The jagged nature of the measured data plot around days 217–223, 2008, is suspected to result from thermal or wind effects on the sensor. Black curve is cumulative ablation for 2007 as calculated by the model. Blue dot with ±15 cm error bar is the only existing automatic sonic ranger measurement. The error bar is the error on the initial mounting height of the sensor at deployment time, 2007, as estimated from photos of the AWS. Shaded area is propagated uncertainty determined by perturbing all measured parameters with uncertainty values provided by instrument manufacturers (see section 2.1.2). (b) Difference between cumulative measured and modeled melt as a function of time, 2008. Note the change in scale.

ablation was ~4 cm higher than the modeled amount. The average difference throughout the deployment is 0.5 cm.

3.1.2. Comparison Between Modeled Melt and Stake Measurements

[55] In 2007, the modeled melt is 0.89 m at the location of the AWS (Figure 5). To measure ablation over the same period, we combined two measurements of ice-surface height relative to the structure of the AWS. The first measurement is an estimate made from photographs of the AWS taken at the time of its deployment. The second is a distance measurement from the AWS sonic ranger obtained at the end of the occupation, on day of year 235 (i.e., 23 August 2007). Unfortunately, the sonic ranger record is missing, except for that day, due to instrument malfunction. Figure 5 shows that the measured ablation (0.85 ± 0.15 m) is consistent with the modeled ablation, 0.89 m. The large uncertainty quoted is due to having resorted to using photographs, which are of significantly lower precision than the sonic ranger. The 2008 sonic ranger record is complete and also plotted in Figure 5 together with one independent stake measurement, made on a field visit on day 213. Bias relative to the stake measurements in both years is consistent, i.e., positive but within the error bars.

[56] We now evaluate the ability of the SEB model to capture spatial variation across Helheim Glacier by comparing modeled melt rates to stake measurements made at the sites occupied by GPS receivers. This comparison focuses on 19 GPS station locations of the 2008 data set, since the AWS record from that year is more complete than that from 2007. The average measured melt rate at the 19 locations is 3.3 ± 1 cm d^{-1}. The relatively large uncertainty associated with the measured melt rates is discussed in section 2.3. Figure 6 shows the modeled and observed melt rates at the 19 sites. Of the 19 sites, observed melt rates at 11 sites are consistent with the modeled melt rates in the same locations within the assigned error. Interestingly, the remaining eight sites (plotted in red) are clustered at low elevation where we expect self-drilling to be most prevalent. The horizontal error bars (i.e., those associated with the modeled melt rates) show the mean of the daily errors calculated as per the error analysis described in section 2.1.2. The errors on the modeled melt rates are within ±13% of the unperturbed model solution.

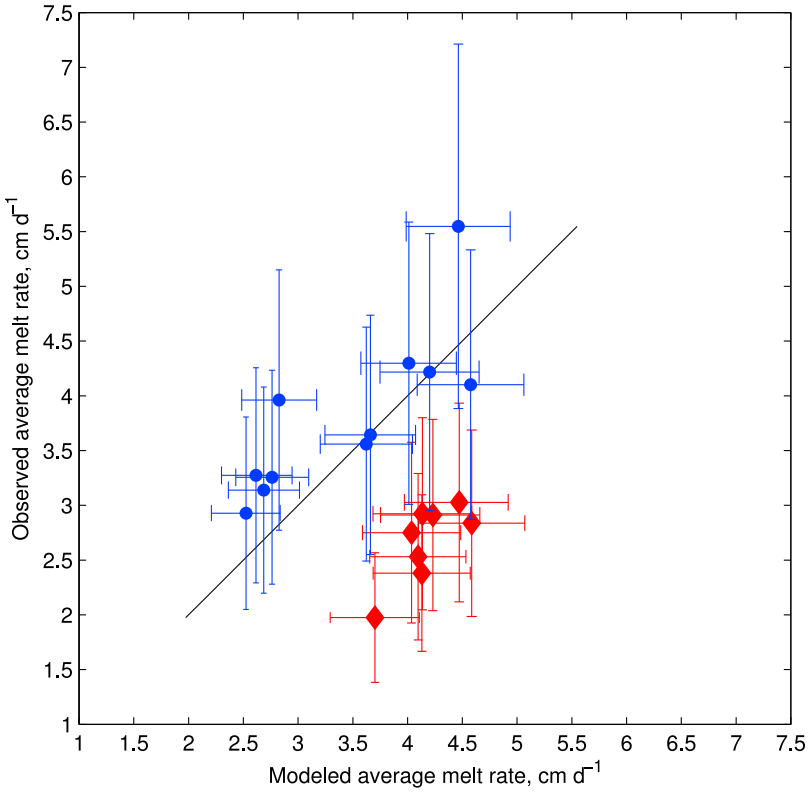

Figure 6. Comparison between measured and modeled melt rates in the model cells where stake measurements were made in 2008. Errors of 30% of the individual measurements are assigned to the stake measurements to account for local variability. Horizontal error bars are errors calculated from the perturbation analysis described in section 2.1.2. Black line traces the values where modeled and observed melt rates are equal. Modeled melt rates that are not statistically consistent with the observed melt rates are plotted with red diamonds. All stations in this group are located in the front cluster, the area where we expect self-drilling to be most prevalent.

3.2. Spatial Distribution of Surface Melt

[57] To investigate the model's ability to capture local variations in melt, separate records are extracted for the grid cells within which the GPS data were recorded. The average positions of each GPS receiver during the deployment are used to identify these cells, which are located both up- and downstream of the AWS.

3.2.1. Integrated Melt

[58] Figure 7 shows the 2007 and 2008 results for the distributed grid, plotted as average melt rates in millimeters per day, water equivalent (mm d^{-1} w.e.). Helheim Glacier exhibits a large altitudinal gradient in melt. Mean melt in the front area is ~63–77% higher than at the upper sites, with average melt rates of 39 and 41 mm d^{-1} w.e. for 2007 and 2008, respectively, over the whole deployment period.

[59] Selected results of the 2007 model run are shown in Figure 8. Figure 8a shows, for the area in Figure 7a, the temporal variation in total melt over the model region ("07Integrated") both in absolute daily volumes and relative to the mean of 1.5×10^7 m^3 d^{-1} w.e. Two distinct periods of increasing melt followed by an abrupt termination are evident, one from day 213 to 217 and one from 220 to 223. Near the end of the deployment period, two single days of large negative deviations from the mean occur on days 230 and 232.

[60] Day-to-day variations in melt in 2008 (relative to the mean for the integrated melt over the model domain, 1.4×10^7 m^3 d^{-1} w.e.) are as much as +68% and −64% (melt record "08Integrated" shown in Figure 9a). A period with small variations around the mean lasts from the beginning of the deployment until day 210. A clear buildup and peak in melting then occurs from day 210 to 219, peaking at day 212. The peak on day 212 (68% higher than the mean) is the highest daily melt in the deployment. This is followed by a period of below-average melt, lasting until the end of the time series.

[61] The assigned error bars in Figures 8a and 9a are averages of the daily errors determined at the 16 specific sites for 2007 and 19 sites for 2008, calculated as a percentage of the average daily melt at these sites. The means of this percentage (i.e., the error) are ±11% and ±13%, for 2007 and 2008 respectively.

3.2.2. Local Melt Records

[62] For 2007 and 2008, we consider a number of local melt records corresponding to the grid cells containing the average position of a given GPS receiver throughout the deployment. We select locations both up- and downstream (2007: IS30 and IS35, respectively; 2008: IS53 and IS42, respectively) (Figure 1). The corresponding melt estimates are "07upstream," "07downstream," "08upstream," and

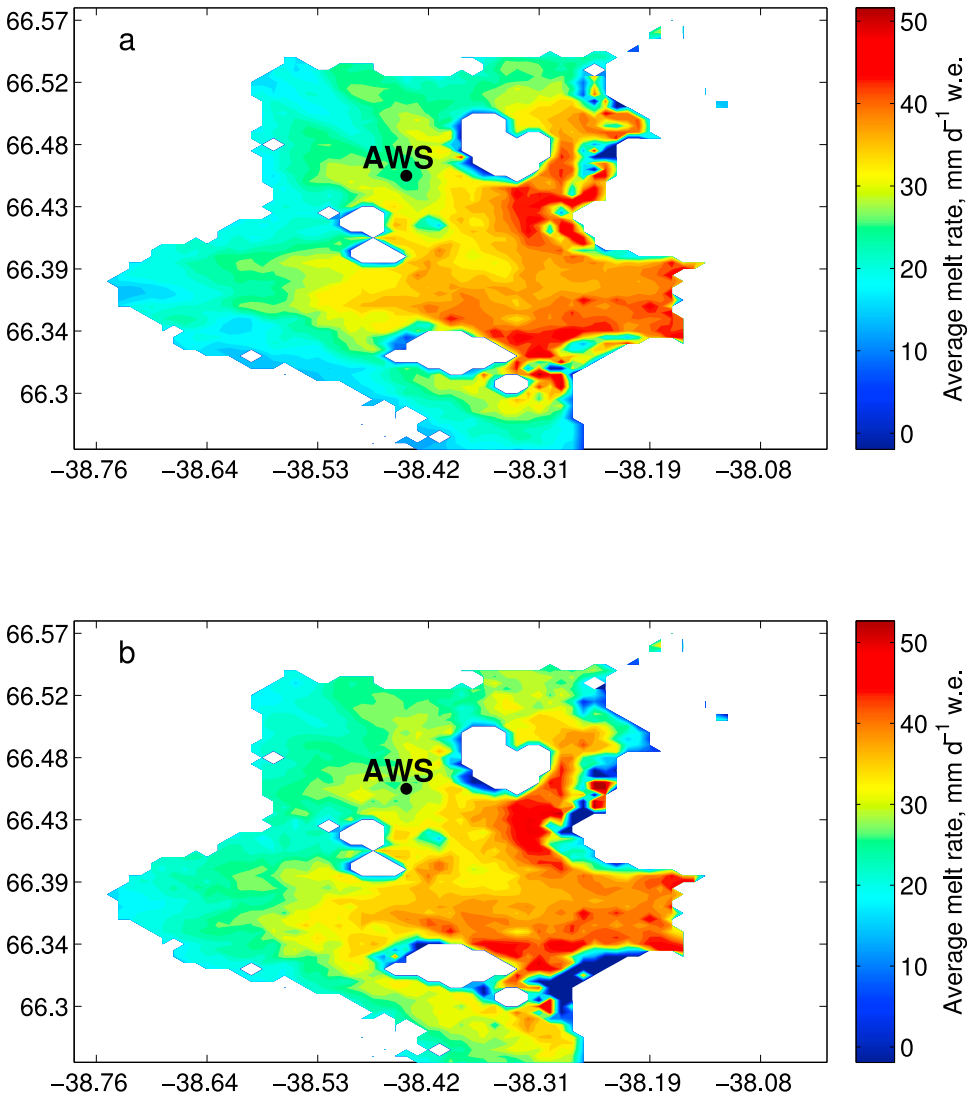

Figure 7. Average melt rate at Helheim Glacier. (a) Days of year 208–235, 2007. (b) Days of year 182–232 for 2008. Black dot indicates position of AWS. Geographic coordinates designate model grid point intersections with ticks for every 10 model cells in each direction. Error in estimated values is typically ±11–13% (see section 3.2.1).

"08downstream," respectively. For model calibration purposes, we also calculate a melt record for the model cell containing the AWS, termed "08AWS."

[63] Figures 8b and 8c show melt records 07upstream and 07downstream, which overall are quite similar. Melt fluctuations from the mean are slightly larger in the 07downstream record with a maximum deviation from the mean of 58%, while the upstream maximum is 55%. Other subtle differences are also evident in the records. For example, melt increases strongly from day 214 to 215 up-glacier, while no change (within error bars) is observed at the front during the same time period.

[64] Similar characteristics are also noted in the 2008 upstream and downstream melt records (Figures 9b and 9c). Here, smaller-scale differences are also apparent. For example, the peak melting occurs 2 days earlier (day 212) at the downstream site compared to the upstream site (day 214). In general, for both years, the pattern of melt calculated at specific locations resembles the pattern seen in the total melt across the glacier.

[65] Mean daily errors upstream are −3.1 and +3.3 mm w.e. for 2007 and −3.4 and +3.5 mm w.e. for 2008 (Figures 8b and 9b), corresponding to approximately ±13% and ±15% of mean melt in the upstream locations, respectively. Mean daily errors downstream are −4.3 and +4.4 mm w.e. for 2007 and −5.3 and +5.0 mm w.e. for 2008 (Figures 8c and 9c), corresponding to ±11% and ±13% of mean downstream melt, respectively.

3.3. Comparison of Melt Rates and Ice Speed Variations

[66] We investigate the potential effect of runoff on flow speed through statistical analyses of the modeled melt records and the observed surface velocities. For 2007 and 2008 we perform local cross-correlation analyses of upstream melt estimates (07upstream/08upstream) with upstream

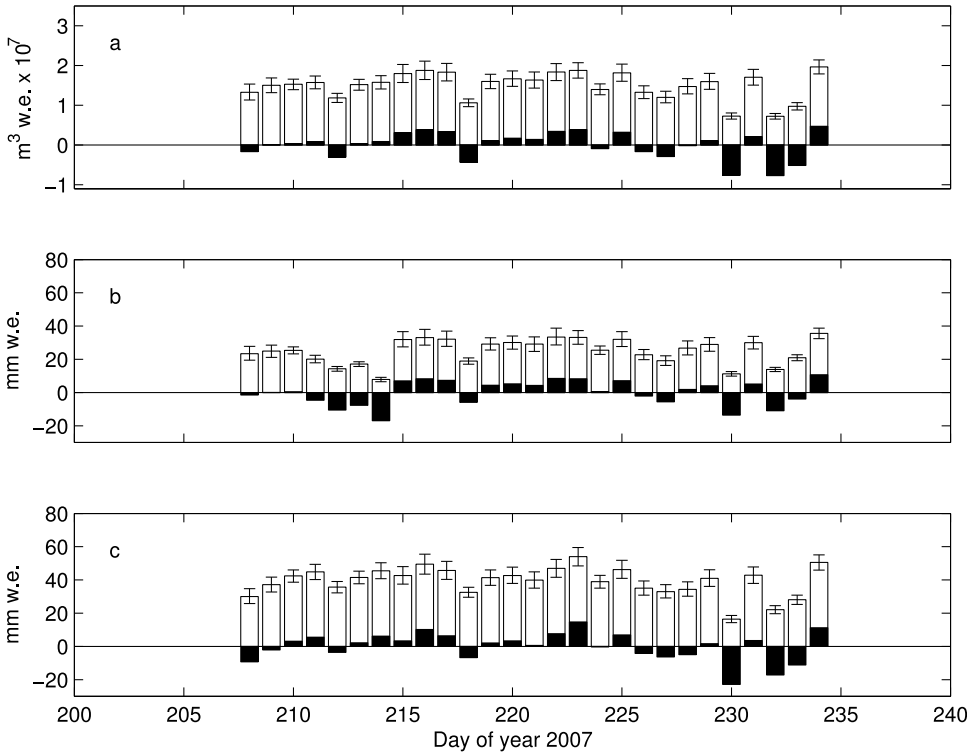

Figure 8. Melt in absolute quantities (white bars) with error bars calculated from the sensitivity analysis (see section 2.1.2), and melt relative to mean (black bars), 2007. (a) Integrated melt over entire model domain (record 07Integrated), with mean value 1.5×10^7 m^3 d^{-1} w.e. (b) Melt calculated in upstream model cell containing average position of GPS station IS30 (record 07upstream), with mean value 24.8 mm d^{-1} w.e. (c) Melt calculated in downstream model cell containing average position of GPS station IS35 (record 07downstream), with mean value 39.3 mm d^{-1} w.e.

velocity records, and the downstream melt estimates (07downstream/08downstream) with downstream velocity records. We also correlate estimates of the total melt, integrated across the entire model domain (07Integrated/08Integrated) to the front area velocities. Finally, we perform a similar analysis using the estimated 2008 melt record from the AWS site (08AWS) since the AWS was colocated with a GPS receiver to within 20 m.

[67] In a qualitative sense, we observe that when the melt is above the mean, the velocity also tends to be above the mean, as can be seen in the top two panels of Figures 10 and 11. This pattern is borne out quantitatively by the results of the cross-correlation analysis.

3.3.1. Summer of 2007

[68] Figure 10a shows the temporal variation of the integrated surface melt record (07Integrated, in blue), the upstream record (07upstream, in red), and the downstream record (07downstream, in green) with respect to mean values of 1.5×10^7 m^3 d^{-1} w.e., 24.8 mm d^{-1} w.e., and 39.3 mm d^{-1} w.e., respectively (see Figure 7). To facilitate comparison between signals, melt variations in the figure are normalized relative to the maximum amplitude in each zero-mean time series. Figure 10b shows the temporal variation of GPS-derived ice velocity for three representative glacier sites (blue for the downstream trunk, green for the front, and red for the upstream sites). Speeds are shown as deviations from the mean, which are 15.6, 23.2, and 12.9 m d^{-1}, respectively. Figure 10c shows correlation coefficients for several values centered around zero lag between matching pairs, that is, between the 07Integrated melt and the ice speed of the frontal station, the 07downstream melt and the speed of the downstream station, and 07upstream melt and the upstream station speed.

[69] The largest correlation coefficients r that result from testing these records for the effect of surface melt on ice speed variations are $r = 0.68$, 0.42, and 0.42, respectively. The correlation coefficients for all three cases peak when the velocity is delayed by 1 day relative to surface melt. (There is a secondary, local maximum at negative delays for the 07upstream/upstream correlation. However, correlation values at negative time delays, which are included for completeness, have no physical meaning.) To evaluate the statistical significance of these correlation values, we first calculate autocorrelation functions for surface melt variations and speed variations to assess the degree of independence, or randomness, of those samples. These tests reveal a decorrelation time of 2 days; we define decorrelation time as the lag beyond which the autocorrelation function falls within the values of a normally distributed function at the 95% confidence limit. Therefore, we reduce the degrees of freedom available to calculate significance from 27, the total number of samples, to 13. The p values for the three correlation coefficients, using 13 degrees of freedom and a one-tailed test (warranted by the hypothesis that ice velocity

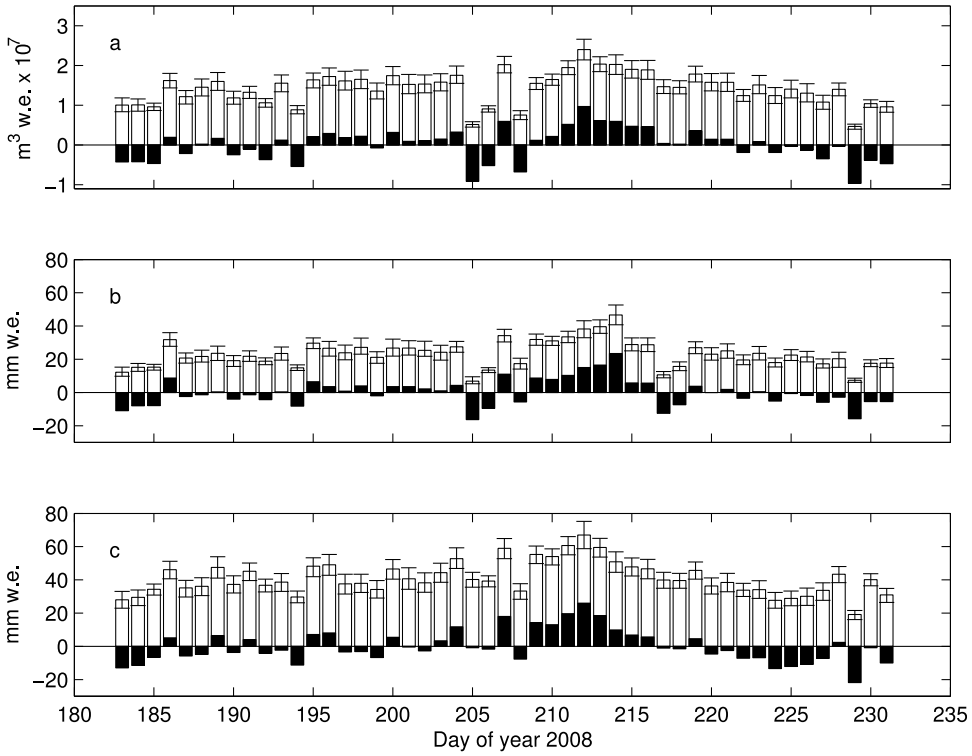

Figure 9. Melt in absolute quantities (white bars) with error bars calculated from the sensitivity analysis (see section 2.1.2), and melt relative to mean (black bars), 2008. (a) Integrated melt over entire model domain (record 08Integrated), with mean value 1.4×10^7 m^3 d^{-1} w.e. (b) Melt calculated in upstream model cell containing average position of GPS station IS53 (record 08upstream), with mean value 23.1 mm d^{-1} w.e. (c) Melt calculated in downstream model cell containing average position of GPS station IS42 (record 08downstream), with mean value 41 mm d^{-1} w.e.

does not affect surface melt), are $p = 0.0068$, 0.0595, and 0.0595, respectively, indicating significant correlations for all three comparisons at >90% levels (IS25, IS30, and IS35), and >99% levels for the comparison involving the integrated melt and ice speed of the downstream trunk area (IS25).

3.3.2. Summer of 2008

[70] Results for the summer of 2008 are consistent with those of 2007. Figure 11a shows surface melt variations, Figure 11b shows ice velocity variations, and Figure 11c shows the correlation values for the comparison of melt records with their respective velocity records. There is a maximum positive correlation coefficient of $r = 0.57$ in the 08Integrated/front area station comparison. As in 2007, the maximum correlation coefficient peak occurs when the velocity signal lags the melt signal by 1 day. The local comparisons yield correlation coefficients of $r = 0.53$ for 08downstream/downstream station and $r = 0.11$ for the 08AWS/AWS station, also with a 1 day delay producing the highest r value. While notably smaller than at the sites on the lower glacier, there is also a distinguishable peak around this coefficient where the surrounding correlation coefficients (±1 day relative to the peak) are $r = -0.09$ and $r = -0.05$, respectively. In the 08upstream/upstream station correlation, an r value of 0.46 occurs with a 1 day delay, consistent with the results at the front of the glacier.

[71] As in the 2007 records, the autocorrelations of surface melt and ice velocity signals yield a decorrelation time of 2 days, or a total of ~24 degrees of freedom, for the $N = 49$ data points (days) in the original records. Since the resulting p values for the comparisons discussed above are $p = 0.0012$, $p = 0.0027$, $p = 0.2963$, and $p = 0.009$, respectively, they reveal correlation coefficients for a 1 day delay that are all statistically significant at >99% levels for all but the 08AWS/AWS velocity record comparison.

4. Discussion

[72] In general, melt/velocity correlation coefficients are comparable for the 2 years of observation. All comparisons in 2007 and 2008 yield the highest correlation coefficients when the velocity is delayed 1 day relative to the melt signal. Adjacent correlation values are significantly smaller, indicative of a well-peaked correlation function. We note that the 2007 melt data are calculated using a synthetic temperature record which is only half the length of the 2008 record, potentially influencing the correlation values. That the 1 day optimal delay is seen everywhere may be related to the overall coherence of the ice body. However, the stronger correlations observed lower on the glacier suggest some spatial dependence in the glacier's response to runoff. For all comparisons, except the 08AWS/AWS velocity record, we see a statistically significant correlation at the 90% level or above (for 2008, 99% levels). We therefore reject the null hypothesis that melt does not have any effect

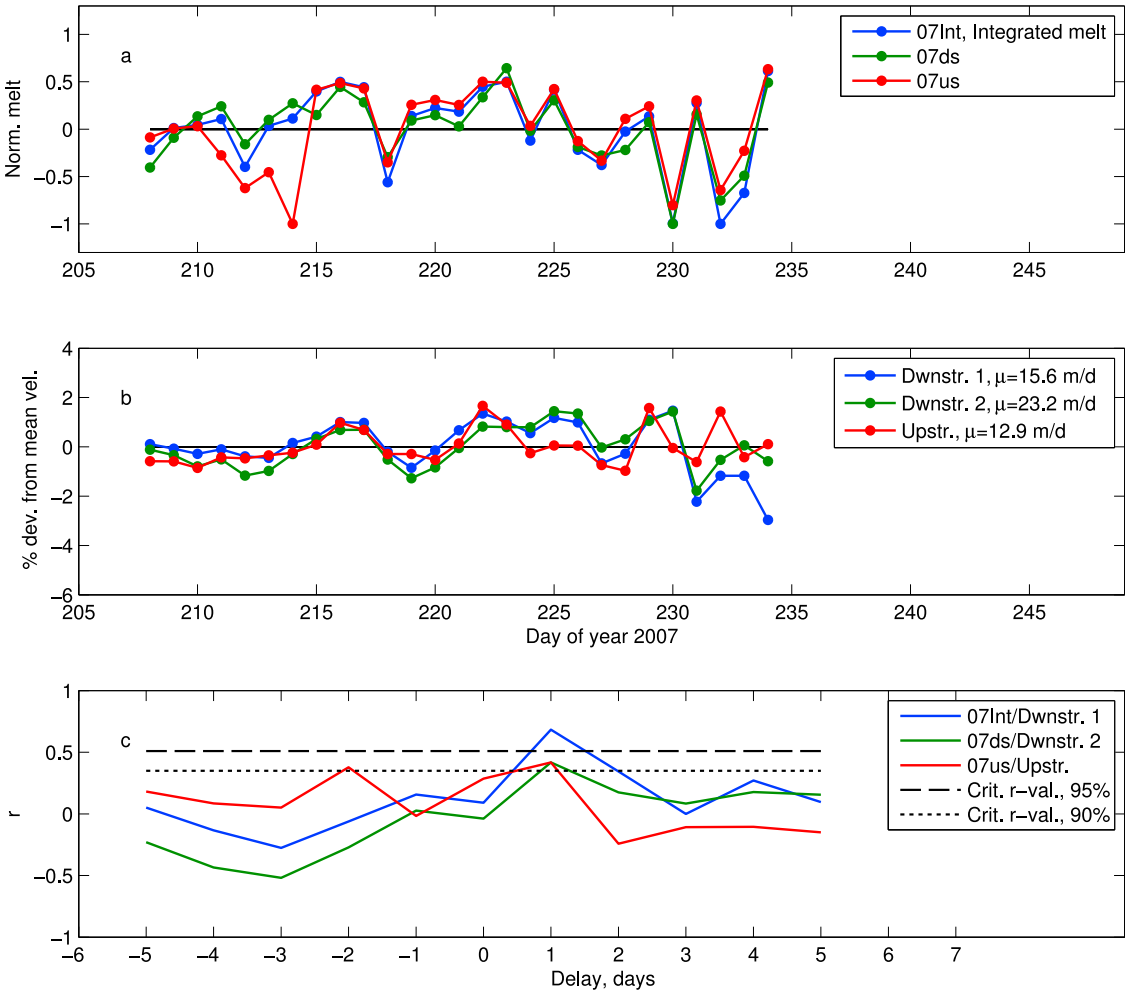

Figure 10. Comparisons of melt and velocity, 2007: (a) Melt signals 07Integrated, 07downstream, and 07upstream. All signals are plotted as deviations from the mean and normalized relative to maximum amplitude for comparison. (b) Deviations from mean measured surface speed at downstream GPS site 1 (IS25), downstream GPS site 2 (IS35), and upstream GPS site (IS30) in percentages. (c) Correlation coefficients for comparisons 07Integrated/downstream 1, 07downstream/downstream 2, and 07upstream/upstream. Dashed line is critical r value ($r = 0.51$) for significance at the 95% level, dotted line is critical r value ($r = 0.35$) for significance at the 90% level. Both with 13 degrees of freedom, one-tailed distribution.

on ice velocity, keeping in mind that even significant correlation does not imply causation.

[73] For both 2007 and 2008, the highest r values result from correlating the integrated daily melt signal with the velocity records representative of the glacier front area. The strong correlation near the front, especially for 2008, suggests that melt affects velocity behavior in a direct way in this area. If the correlation coefficient can be interpreted as a measure of the strength of the effect of melt on velocity, our results indicate that this effect is stronger near the front of the glacier than farther upstream. There are several reasons this may be the case. The front of Helheim Glacier is heavily crevassed because of high strain rates (~0.5 yr^{-1}). We suggest that the strain rate field creates conditions favorable for the rapid transit of runoff from the surface to the bed. This region of the glacier is near flotation [*de Juan et al.*, 2010] and is probably sensitive to additional surface meltwater perturbing the already high basal water pressure. Conversely, we see lower correlation values in the areas where the surface velocities are slower, for example by stations IS51 and IS53, 2008 (Figure 1b). The station farthest upstream, IS53, has a higher average velocity than the station downstream of it, IS51, indicating the existence of a compression zone between the two sites. The correlation of the melt and the velocity signals is lower at IS51 (AWS site) than at any other site considered in 2008. We note, however, that the up-glacier sites are at higher altitudes where less melt is generated, possibly limiting the effect of basal lubrication.

[74] With our daily time resolution of the velocity record, our results point to a delay of 12–36 h from generation at the surface to the time when an effect is observed. We expect the time lag to be closer to 12 h than 36 h, which is still longer than the response times found on the ice sheet flank by, e.g., *Shepherd et al.* [2009].

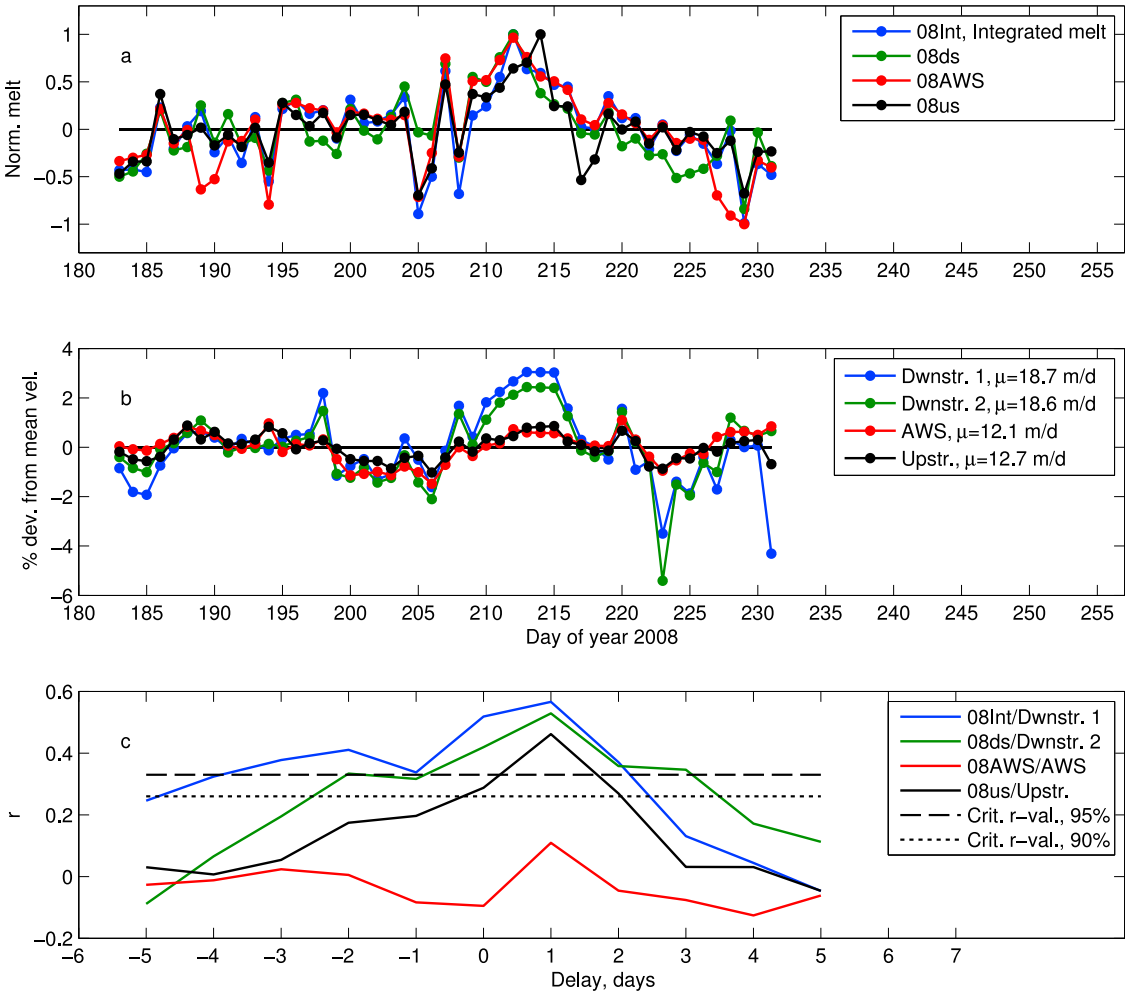

Figure 11. Comparisons of melt and velocity, 2008: (a) Melt signals 08Integrated, 08downstream, 08AWS, and 08upstream. All signals are plotted as deviations from the mean and normalized relative to maximum amplitude for comparison. (b) Deviations from mean measured surface speed at downstream GPS site 1 (IS41), downstream GPS site 2 (IS42), AWS GPS site (IS51), and upstream GPS site (IS53) in percentages. (c) Correlation coefficients for comparisons 08Integrated/downstream 1, 08downstream/downstream 2, 08AWS/AWS, and 08upstream/upstream. Dashed line is critical r value (r = 0.33) for significance at the 95% level, dotted line is critical r value (r = 0.26) for significance at the 90% level. Both with 24 degrees of freedom, one-tailed distribution.

[75] The full range of velocity variations for the time series shown in Figures 10 and 11, after the effects of glacial earthquakes and advection have been removed, is about +3% to −5.5%, with typical variations of about ±2%. For the 2% case, the corresponding absolute velocity variations range from about 0.2–0.5 m d^{-1} or ~70–180 m yr^{-1}. *Joughin et al.* [2008b] find meltwater-induced velocity variations on West Greenland outlet glaciers (Jakobshavn Isbræ and a number of smaller, marine terminating glaciers in this region), determined in 24 day averages, to be about half this large. For the purpose of comparison, we produce twenty-nine 24 day running averages for our daily 2008 time series centered on days 10 July–7 August (days of year 192–220). We use station IS41, close to the glacier front, for the comparison: this station has a mean daily velocity of 18.4 m d^{-1} after corrections for glacial earthquakes and advection have been applied. The 24 day averaging naturally smoothes day-to-day variations and yields a peak difference between the seasonal mean speed and the highest 24 day average speed of ~1%, corresponding to a variability of ~55 m yr^{-1}, i.e., within the 51–77 m yr^{-1}reported by *Joughin et al.* [2008b] in West Greenland. We therefore believe our results to be generally in good agreement with those of *Joughin et al.* [2008b] and note that daily variations in speed due to runoff do not differ dramatically in amplitude from the seasonal.

[76] Our knowledge of Helheim Glacier's water budget is incomplete because no record of discharge exists. We also lack information on basal water pressures and storage times, data usually acquired by drilling to the bed or through dye-tracing experiments [e.g., *Kamb et al.*, 1985]. It is therefore not possible at this point to determine if Helheim's subglacial hydrology is dominated by a low-pressure tunnel system, a system of distributed linked cavities and small

channels, or both [see, e.g., *Kamb et al.*, 1985; *Kamb*, 1987; *Björnsson*, 1998; *Bartholomaus et al.*, 2008].

[77] Above-normal runoff due to surface melt near the front of the glacier can have an effect in filling crevasses and accelerating calving processes, causing accelerations of the glacier trunk, as described by *Sohn et al.* [1998]. Enhanced calving by hydrofracturing has been modeled by *Benn et al.* [2007]. As demonstrated by *Nettles et al.* [2008], the glacier dynamics observed in the GPS signals are modulated partly by calving at the front, coeval with glacial earthquakes. We observe that, of the seismic events occurring within the period of melt calculation in 2007, two occur on day 225, 2 days after the maximum melt observed. The same pattern is seen in 2008, when on day 214 two glacial earthquakes were detected, again2 days after a period of strong meltwater production. This suggests a relationship between melt output and calving. However, in 2008, a glacial earthquake also occurred on day 232 following several days of below-mean melt. The relatively short time series used and the small sample size in this study is thus insufficient to test this intriguing hypothesis.

5. Conclusions

[78] We have developed a distributed surface-energy-balance model for Helheim Glacier and validated it against field observations for 2008. The model was run over a period of 27 full days for 2007 and 49 full days for 2008 to estimate daily runoff from surface melt over the snow-free part of the glacier (i.e., below 1000 m above sea level). The calibrated model performed well and produced results in agreement with ablation observations made at an AWS on the glacier.

[79] Estimated melt rates are similar for both years. Average modeled melt rates for the grid cell containing the AWS were 3.2 cm d^{-1} (~29.0 mm d^{-1} w.e.) for 2007 and 2008. Average melt rates for the frontal area of the glacier are 4.44 cmd^{-1} (40.7 mm d^{-1} w.e.) and 4.36 cm d^{-1} (40.0 mm d^{-1} w.e.) for 2007 and 2008, respectively. Up-glacier of the AWS, modeled melt rates are 2.42 cm d^{-1} (22.2 mm d^{-1} w.e.) in 2007 and 2.24 cm d^{-1} (20.5 mm d^{-1} w.e.) in 2008 for the entire deployment periods. The slightly lower melt rates in 2008 are mainly due to the time series starting earlier in the melt season when melt rates were lower.

[80] The melt signal at Helheim has a large altitudinal gradient, which can partly be ascribed to the elevation difference of ~900 m between the glacier front and the up-glacier part of the catchment. Variations in albedo also contribute to the spatial differences in melt, with the lower, heavily crevassed, reaches of the glacier having lower albedo.

[81] Total melt output and model results from selected cells are correlated with observations of speed from GPS network deployments on Helheim Glacier in 2007 and 2008. The highest correlations occur for locations near the front of the glacier in both years. For all comparisons but one, we find that the correlations are significant at >90% levels. For both years, 12–36 h delays between meltwater generation at the surface and glacier speed increases are found. We suggest that the lower bound of this interval represents the transition time for runoff to travel from the surface to the bed of the glacier, while acknowledging that our 1 day temporal resolution may influence this interpretation.

[82] Our results indicate a dependence of ice velocity on runoff variations at a fast-flowing outlet glacier. The effect is larger near the front of the glacier where melt rates are higher. We argue that part of the spatial dependence of this effect is caused by the difference in the magnitude of the meltwater flux. However, we also speculate that the enhanced response near the front results from this region having a better hydraulic connection to the bed, thereby supplying additional water at a faster rate. Moreover, a large fraction of the generated runoff from the entire catchment is expected to be routed under the frontal area of the glacier, possibly causing a cumulative dynamic effect.

[83] While large accelerations, primarily at the front of the glacier, are governed by calving dynamics [e.g., *Nettles et al.*, 2008], it is clear from this study that variations in runoff volume contribute to the velocity behavior of Helheim Glacier. Temporally coincident large melt fluxes and calving events suggest that basal water lubrication might bring the glacier into a calving-prone state, but further research is required to test this hypothesis.

[84] **Acknowledgments.** The Helheim 2007 and 2008 project was supported by the Gary Comer Science and Education Foundation, the U.S. National Science Foundation, the Danish Commission for Scientific Research in Greenland (KVUG), the Spanish Ministry of Science and Innovation (MICINN), the Geological Survey of Denmark and Greenland (GEUS), Geocenter Copenhagen, the Danish National Space Center, NASA, the Lamont-Doherty Climate Center, and the Dan and Betty Churchill Exploration Fund. GPS equipment and technical support were provided by UNAVCO, Inc. The authors thank Dr. Michele Citterio, GEUS, for GIS assistance. The authors thank Martin Truffer (Associate Editor), Timothy C. Bartholomaus, and three anonymous reviewers for constructive reviews that helped improve the manuscript.

References

Amundson, J. M., M. Truffer, M. P. Luethi, M. Fahnestock, M. West, and R. J. Motyka (2008), Glacier, fjord, and seismic response to recent large calving events, Jakobshavn Isbrae, Greenland, *Geophys. Res. Lett.*, *35*, L22501, doi:10.1029/2008GL035281.

Bartholomaus, T. C., R. S. Anderson, and S. P. Anderson (2008), Response of glacier basal motion to transient water storage, *Nat. Geosci.*, *1*(1), 33–37, doi:10.1038/ngeo.2007.52.

Benn, D. I., C. R. Warren, and R. H. Mottram (2007), Calving processes and the dynamics of calving glaciers, *Earth-Sci. Rev.*, *82*(3–4), 143–179, doi:10.1016/j.earscirev.2007.02.002.

Björnsson, H. (1998), Hydrological characteristics of the drainage system beneath a surging glacier, *Nature*, *395*(6704), 771–774.

Braithwaite, R. (1995), Positive degree-day factors for ablation on the Greenland Ice-sheet studied by energy-balance modeling, *J. Glaciol.*, *41*(137), 153–160.

Brock, B. W., I. C. Willis, and M. J. Shaw (2006), Measurement and parameterization of aerodynamic roughness length variations at Haut Glacier d'Arolla, Switzerland, *J. Glaciol.*, *52*(177), 281–297.

de Juan, J., et al. (2010), Sudden increase in tidal response linked to calving and acceleration at a large Greenland outlet glacier, *Geophys. Res. Lett.*, *37*, L12501, doi:10.1029/2010GL043289.

Ettema, J., M. R. van den Broeke, E. van Meijgaard, W. J. van de Berg, J. L. Bamber, J. E. Box, and R. C. Bales (2009), Higher surface mass balance of the Greenland ice sheet revealed by high-resolution climate modeling, *Geophys. Res. Lett.*, *36*, L12501, doi:10.1029/2009GL038110.

Greuell, W., and T. Konzelmann (1994), Numerical Modeling of the energy balance and the englacial temperature of the Greenland Ice-sheet: Calculations for the ETH-Camp location (West Greenland, 1155 m asl), *Global Planet. Change*, *9*(1–2), 91–114.

Hall, D. K., G. A. Riggs, and V. V. Salomonson (2007), MODIS/Terra Snow Cover Daily L3 Global 500m Grid V005, Julian days 205, 209, 218, 222, 224, 225, 227, 228, 230, 234. Updated daily, http://nsidc.org/data/index.html.

Hall, D. K., G. A. Riggs, and V. V. Salomonson (2008), MODIS/Terra Snow Cover Daily L3 Global 500m Grid V005, Julian days 179, 180, 182, 183, 195, 199, 200, 202, 203, 204, 205, 207, 209, 214, 216, 217,

218, 222, 223, 225, 235, 238. Updated daily, http://nsidc.org/data/index.html.

Hanna, E., P. Huybrechts, I. Janssens, J. Cappelen, K. Steffen, and A. Stephens (2005), Runoff and mass balance of the Greenland ice sheet: 1958–2003, *J. Geophys. Res.*, *110*, D13108, doi:10.1029/2004JD005641.

Hock, R. (2005), Glacier melt: A review of processes and their modelling, *Prog. Phys. Geogr.*, *29*(3), 362–391.

Hock, R., and B. Holmgren (2005), A distributed surface energy-balance model for complex topography and its application to Storglaciären, Sweden, *J. Glaciol.*, *51*(172), 25–36.

Holtslag, A. A. M., and H. A. R. De Bruin (1988), Applied modeling of the nighttime surface-energy balance over land, *J. Appl. Meteorol.*, *27*(6), 689–704.

Howat, I. M., I. Joughin, and T. A. Scambos (2007), Rapid changes in ice discharge from Greenland outlet glaciers, *Science*, *315*(5818), 1559–1561, doi:10.1126/science.1138478.

Howat, I. M., I. Joughin, M. Fahnestock, B. E. Smith, and T. A. Scambos (2008a), Synchronous retreat and acceleration of southeast Greenland outlet glaciers 2000–06: Ice dynamics and coupling to climate, *J. Glaciol.*, *54*(187), 646–660.

Howat, I. M., S. Tulaczyk, E. Waddington, and H. Björnsson (2008b), Dynamic controls on glacier basal motion inferred from surface ice motion, *J. Geophys. Res.*, *113*, F03015, doi:10.1029/2007JF000925.

Huybrechts, P., A. Letreguilly, and N. Reeh (1991), The Greenland Ice-sheet and greenhouse warming, *Global Planet. Change*, *89*(4), 399–412.

Iken, A., and R. Bindschadler (1986), Combined measurements of subglacial water-pressure and surface velocity of Findelengletscher, Switzerland: Conclusions about drainage system and sliding mechanism, *J. Glaciol.*, *32*(110), 101–119.

Joughin, I., I. Howat, R. B. Alley, G. Ekstrom, M. Fahnestock, T. Moon, M. Nettles, M. Truffer, and V. C. Tsai (2008a), Ice-front variation and tidewater behavior on Helheim and Kangerdlugssuaq Glaciers, Greenland, *J. Geophys. Res.*, *113*, F01004, doi:10.1029/2007JF000837.

Joughin, I., S. B. Das, M. A. King, B. E. Smith, I. M. Howat, and T. Moon (2008b), Seasonal speedup along the western flank of the Greenland Ice Sheet, *Science*, *320*(5877), 781–783, doi:10.1126/science.1153288.

Joughin, I., I. M. Howat, M. Fahnestock, B. Smith, W. Krabill, R. B. Alley, H. Stern, and M. Truffer (2008c), Continued evolution of Jakobshavn Isbrae following its rapid speedup, *J. Geophys. Res.*, *113*, F04006, doi:10.1029/2008JF001023.

Kamb, B. (1987), Glacier surge mechanism based on linked cavity configuration of the basal water conduit system, *J. Geophys. Res.*, *92*(B9), 9083–9100.

Kamb, B., C. Raymond, W. Harrison, H. Engelhardt, K. Echelmeyer, N. Humphrey, M. Brugmann, and T. Pfeffer (1985), Glacier surge mechanism: 1982–1983 surge of Variegated Glacier, Alaska, *Science*, *227*(4686), 469–479.

Liston, G., and K. Elder (2006), A meteorological distribution system for high-resolution terrestrial modeling (MicroMet), *J. Hydrometeorol.*, *7*(2), 217–234.

Luckman, A., and T. Murray (2005), Seasonal variation in velocity before retreat of Jakobshavn Isbrae, Greenland, *Geophys. Res. Lett.*, *32*, L08501, doi:10.1029/2005GL022519.

Luckman, A., T. Murray, R. de Lange, and E. Hanna (2006), Rapid and synchronous ice-dynamic changes in East Greenland, *Geophys. Res. Lett.*, *33*, L03503, doi:10.1029/2005GL025428.

MacWhorter, M., and R. Weller (1991), Error in measurements of incoming shortwave radiation made from ships and buoys, *J. Atmos. Oceanic Technol.*, *8*(1), 108–117.

Meesters, A., N. Bink, H. Vugts, F. Cannemeijer, and E. Henneken (1997), Turbulence observations above a smooth melting surface on the Greenland ice sheet, *Boundary Layer Meteorol.*, *85*(1), 81–110.

Mernild, S. H., G. E. Liston, C. A. Hiemstra, and K. Steffen (2008), Surface melt area and water balance modeling on the Greenland Ice Sheet 1995–2005, *J. Hydrometeorol.*, *9*(6), 1191–1211, doi:10.1175/2008JHM957.1.

Munro, D. (1989), Surface-roughness and bulk heat-transfer on a glacier - comparison with eddy-correlation, *J. Glaciol.*, *35*(121), 343–348.

Nettles, M., et al. (2008), Step-wise changes in glacier flow speed coincide with calving and glacial earthquakes at Helheim Glacier, Greenland, *Geophys. Res. Lett.*, *35*, L24503, doi:10.1029/2008GL036127.

Nick, F. M., A. Vieli, I. Howat, and I. Joughin (2009), Large-scale changes in Greenland outlet glacier dynamics triggered at the terminus, *Nat. Geosci.*, *2*, 110–114, doi:10.1038/ngeo394.

Paulson, C. A. (1970), The Mathematical Representation of Wind Speed and Temperature Profiles in the Unstable Atmospheric Surface Layer, *J. Appl. Meteorol.*, *9*(6), 851–856.

Reeh, N. (1991), Parameterization of melt rate and surface temperature, *Polarforschung*, *59*(3), 113–128.

Rignot, E., and P. Kanagaratnam (2006), Changes in the velocity structure of the Greenland ice sheet, *Science*, *311*(5763), 986–990, doi:10.1126/science.1121381.

Shepherd, A., A. Hubbard, P. Nienow, M. King, M. McMillan, and I. Joughin (2009), Greenland ice sheet motion coupled with daily melting in late summer, *Geophys. Res. Lett.*, *36*, L01501, doi:10.1029/2008GL035758.

Sohn, H., K. Jezek, and C. van der Veen (1998), Jakobshavn Glacier, West Greenland: 30 years of spaceborne observations, *Geophys. Res. Lett.*, *25*(14), 2699–2702.

Stearns, L. A. (2007), Outlet glacier dynamics in East Greenland and East Antarctica, Ph.D. thesis, University of Maine.

Stearns, L. A., and G. S. Hamilton (2007), Rapid volume loss from two East Greenland outlet glaciers quantified using repeat stereo satellite imagery, *Geophys. Res. Lett.*, *34*, L05503, doi:10.1029/2006GL028982.

Stearns, L. A., G. S. Hamilton, and N. Reeh (2005), Multi-decadal record of ice dynamics on Daugaard Jensen Gletscher, East Greenland, from satellite imagery and terrestrial measurements, in *Annals of Glaciology*, vol. 42, edited by J. Dowdeswell and I. C. Willis, pp. 53–58, International Glaciological Society, Cambridge, U.K.

Stroeve, J. C., J. E. Box, and T. Haran (2006), Evaluation of the MODIS (MOD10A1) daily snow albedo product over the Greenland ice sheet, *Remote Sens. Environment*, *105*(2), 155–171, doi:10.1016/j.rse.2006.06.009.

van As, D., M. van den Broeke, C. Reijmer, R. van De Wal (2005), The summer surface energy balance of the high Antarctic plateau, *Boundary Layer Meteorol.*, *115*(2), 289–317, doi:10.1007/s10546-004-4631-1.

van de Wal, R., and J. Oerlemans (1994), An energy-balance model for the Greenland Ice-sheet, *Global Planet. Change*, *9*(1–2), 115–131.

van de Wal, R. S. W., W. Boot, M. R. van den Broeke, C. J. P. P. Smeets, C. H. Reijmer, J. J. A. Donker, and J. Oerlemans (2008), Large and rapid melt-induced velocity changes in the ablation zone of the Greenland Ice Sheet, *Science*, *321*(5885), 111–113, doi:10.1126/science.1158540.

van den Broeke, M., D. van As, C. Reijmer, and R. van de Wal (2004), Assessing and improving the quality of unattended radiation observations in Antarctica, *J. Atmos. Oceanic Technol.*, *21*(9), 1417–1431.

van den Broeke, M., P. Smeets, J. Ettema, C. van der Veen, R. van der Wal, and J. Oerlemans (2008), Partitioning of melt energy and melt water fluxes in the ablation zone of the west Greenland ice sheet, *The Cryosphere*, *2*, 179–189.

Zwally, H., W. Abdalati, T. Herring, K. Larson, J. Saba, and K. Steffen (2002), Surface melt-induced acceleration of Greenland ice-sheet flow, *Science*, *297*(5579), 218–222.

A. P. Ahlstrøm, M. L. Andersen, T. B. Larsen, and D. van As, Geological Survey of Denmark and Greenland (GEUS), Øster Voldgade 10, DK-1350 Copenhagen K, Denmark. (mola@geus.dk)

D. Dahl-Jensen, Centre for Ice and Climate, University of Copenhagen, Juliane Maries Vej 30, DK-2100 Copenhagen Ø, Denmark.

J. L. Davis, G. Ekström, and M. Nettles, Lamont-Doherty Earth Observatory, Columbia University, 61 Rte. 9W, P.O. Box 1000, Palisades, NY 10964-8000, USA.

J. de Juan and P. Elosegui, Institute for Space Sciences, CSIC, IEEC, Gran Capita 2, E-08034 Barcelona, Spain.

R. Forsberg, S. A. Khan, and L. Stenseng, Technical University of Denmark, Juliane Maries vej 30, Bldg. Rockefeller, Rm. 269, DK-2100 Copenhagen Ø, Denmark.

G. S. Hamilton, Climate Change Institute, University of Maine, 4 Sawyer Annex, Orono, ME 04469, USA.

L. A. Stearns, Department of Geology, University of Kansas, 1475 Jayhawk Blvd., Lawrence, KS 66045, USA.